# Pressurized Fluid Damping of Nanoelectromechanical Systems

Oleksiy Svitelskiy,[1,2] Vince Sauer,[1] Ning Liu,[2] Kar-Mun Cheng,[1,*] Eric Finley,[1] Mark R. Freeman,[1,2] and Wayne K. Hiebert[1]

[1]*National Institute for Nanotechnology, Edmonton, Alberta T6G 2M9, Canada*
[2]*Department of Physics, University of Alberta, Edmonton, Alberta T6G 2G7, Canada*

(Received 18 June 2009; published 7 December 2009; corrected 14 December 2009)

Interactions of nanoscale structures with fluids are of current interest both in the elucidation of fluid dynamics at these small scales, and in determining the ultimate performance of nanoelectromechanical systems outside of vacuum. We present a comprehensive study of nanomechanical damping in three gases (He, $N_2$, $CO_2$), and liquid $CO_2$. Resonant dynamics in multiple devices of varying size and frequency is measured over 10 decades of pressure (1 mPa – 20 MPa) using time-domain stroboscopic optical interferometry. The wide pressure range allows full exploration of the regions of validity of Newtonian and non-Newtonian flow damping models. Observing free molecular flow behavior extending above 1 atm, we find a fluid relaxation time model to be valid throughout, but not beyond, the non-Newtonian regime, and a Newtonian flow vibrating spheres model to be valid in the viscous limit.

DOI: 10.1103/PhysRevLett.103.244501 PACS numbers: 47.61.Fg, 47.50.Ef, 62.25.Jk, 85.85.+j

Nanoelectromechanical systems (NEMS) are poised to impact a range of fields from medicine and life sciences to energy and environment to information and communications technology. Touted for their exquisite sensitivity, devices have reached incredible milestones (see, e.g., Ref. [1], and references therein). However, to fully unlock the NEMS potential, understanding of their operation in fluidic environment is needed. Device quality factor $Q$, influenced by environment, directly impacts sensitivity and has emerged as a critical area of study, particularly for biosensing applications [2] and for operation in hostile environments [3].

At the same time, NEMS have emerged as an experimental test bed for studying nanoscale fluid dynamics [4–13]. At larger size scales, the transition from rarified to continuum flow is known to be manifest as changes in the damping behavior of mechanically resonant objects typified by several signature regions in $Q$ vs $P$ plots [4]. An attempt to build a general theory covering all the regions [7] was successful only in the limit of thin long beams [8,14], while the case of rectangular-shaped beams remains controversial. The most complex and most physically interesting of the damping regimes is the crossover occurring when the mean free path in the gas $\lambda_{\mathrm{mfp}}$ is of order of the width of the device $w$ (characteristic length scale), that is, when the Knudsen number, $\mathrm{Kn} = \lambda_{\mathrm{mfp}}/w \sim 1$ [5]. Alternatively, it may be described as when the mechanical oscillation angular frequency $\omega = 2\pi f$ is approximately the inverse of some characteristic relaxation time of the fluid flow $\tau$, that is, when the Weissenberg number $\mathrm{Wi} = \omega\tau \sim 1$ [6]. By virtue of their small size, the crossover in NEMS often occurs at atmospheric pressure or above. While nanoscale device-fluid interactions have been measured up to 1 atm [11–13], overpressures combined with the difficulty of transducing highly damped NEMS signals have presented a technical challenge to observing experimental data in the upper crossover and viscous pressure regimes in NEMS devices. Yet such data are crucial, both for verifying damping behavior for improved device performance and for validating nanoscale oscillatory fluid models [5,6,8–10]. Stroboscopic optical interferometry of NEMS devices [15] allows elucidation of highly damped, and even overdamped device operation. Coupling this technique with a specially designed high-pressure optical chamber [16] has allowed us to investigate the crossover and enter the viscous regime in a broad range of NEMS.

In this Letter, we present a comprehensive study, from vacuum to 20 MPa, of the room temperature pressure behavior of NEMS devices with frequencies ranging from 10 to 250 MHz, in 3 gases (He, $N_2$, and $CO_2$), and in liquid $CO_2$. We find that the Yakhot-Colosqui theory (YCT) [6,13] can adequately describe the behavior in the low $P$ regime up through the crossover (for values of $\omega\tau \gtrsim 0.1$) but ceases to be effective in the viscous regime. The $\tau$ values found by fitting to YCT are larger and vary by gas differently than expected from fundamental considerations. In the viscous regime, including the liquid state, the data can be fit by the model of vibrating spheres (MVS) [9]. Transition between validity of YCT and MVS models occurs around $\mathrm{Kn} \sim 0.05$.

The NEMS, cantilevers, and bridges, were made by top-down patterning of standard silicon-on-insulator wafers. To facilitate capacitive excitation of oscillations with 50 V electric pulses between device and substrate, the top surfaces were coated with ~30 nm of Al [15]. An electron micrograph of a typical device is shown in the inset in Fig. 1. Parameters of the devices are summarized in Table I. Vacuum values of their frequencies $f_0$ matched the expected values [17]. Figure 1 shows the response of a resonator to a pulse arriving at time $t = 0$. The oscillations

 

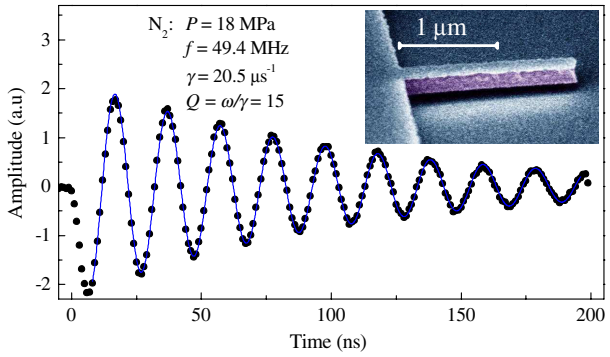


FIG. 1 (color online). Real time free ring down of cantilever 2; circles show measured data, line represents a damped harmonic oscillator fit to experiment. The inset shows the scanning electron micrograph of this device.

amplitude can be fit by the damped harmonic oscillator $A = A_0 e^{-\gamma t/2} \sin(2\pi f t + \phi)$, where $A_0$ and $\phi$ are the initial amplitude and phase; $\gamma$ is damping.

The pressure dependence of a sample device, measured in 3 gases, is shown in Fig. 2. The right inset represents a canonical expectation for the $Q$ behavior [4,9]. At lowest pressure, $Q$ is dominated by intrinsic resonator losses and is constant with $P$. At moderately low $P$, $Q$ decreases as $P^{-1}$ due to momentum exchange with noninteracting gas molecules. At high $P$, $Q$ is determined by losses to a viscous Newtonian fluid and should reach an asymptote of $P^{-1/2}$. The solid curves in the main figure are plots in free molecular flow (FMF) approximation:

$$1/Q = 1/Q_{\text{intrinsic}} + 1/Q_{\text{FMF}}, \quad Q_{\text{FMF}} = \omega m/(2\rho_f U w L), \tag{1}$$

TABLE I. List of investigated samples.

| No. | Type[a] | $w \times d_{\text{Si}} \times L$ ($\mu$m)[b] | $h$ ($\mu$m) | $f_0$ (MHz)[c] |
|---|---|---|---|---|
| 1 | c | 0.25 × 0.147 × 2.00 | 0.139 | 42.8 |
| 2 | c | 0.25 × 0.147 × 1.75 | 0.139 | 54.1 |
| 3 | c | 0.25 × 0.147 × 1.50 | 0.139 | 73.5 |
| 4 | c | 0.25 × 0.147 × 1.25 | 0.139 | 101.2 |
| 5 | c | 0.25 × 0.147 × 1.00 | 0.139 | 161.8 |
| 6 | b | 0.25 × 0.147 × 3.00 | 0.139 | 106.1 |
| 7 | b | 0.25 × 0.147 × 2.75 | 0.139 | 131.7 |
| 8 | c | 0.15 × 0.147 × 2.00 | 0.139 | 41.4 |
| 9 | c | 0.15 × 0.147 × 1.80 | 0.139 | 51.2 |
| 10 | c | 0.15 × 0.147 × 1.60 | 0.139 | 64.3 |
| 11 | c | 0.15 × 0.147 × 1.40 | 0.139 | 82.2 |
| 12 | c | 0.15 × 0.147 × 1.20 | 0.139 | 112.8 |
| 13 | c | 0.15 × 0.147 × 1.00 | 0.139 | 157.6 |
| 14 | c | 0.15 × 0.147 × 0.90 | 0.139 | 191.1 |
| 15 | b | 0.15 × 0.147 × 5.00 | 0.139 | 41.0 |
| 16 | b | 0.15 × 0.147 × 4.00 | 0.139 | 62.4 |
| 17 | b | 0.15 × 0.147 × 3.00 | 0.139 | 116.9 |
| 18 | b | 0.15 × 0.147 × 2.00 | 0.139 | 248.5 |
| 19 | b | 1.00 × 0.188 × 12.0 | 0.372 | 11.5 |

[a]Cantilever (c) or bridge (b).
[b]Width × Si thickness × length
[c]Measured in vacuum.

where $\rho_f$ is the fluid mass density, $U$ is the root-mean-square velocity of the molecules, and $m$ is a device mass. Up to the crossover this parameterless model nicely explains the data for all three gases (also confirming [11,12], obtained in $N_2$ only); 1 dB departure of the data from theory occurs at Kn ~ 0.2. At the highest pressures, the $N_2$ case is approaching the expected asymptote, but not yet the He (on account of lower density) or $CO_2$ data (interrupted by a phase change). Note that the FMF in Fig. 2 continues above 1 atm. In order to shed light on the crossover and viscous regime behavior, data well above atmospheric pressure are necessary. The remainder of this Letter is dedicated to these higher pressure regimes.

Of the two theoretical attempts to unite different pressure regimes, [5] predicts an unphysical discontinuity at the crossover, so we concentrate on the YCT [6], whose preliminary tests made on several devices [13] up to 0.13 MPa covered the crossover only partially. Our data span far beyond the crossover and establish the high-$P$ limit of YCT validity. Developed from the Boltzmann equation in the relaxation time approximation, YCT assumes that the gas-device interaction is described by $\text{Wi} = \omega\tau$, where fluid relaxation time $\tau = \mu_Y/P$ is determined by the Yakhot parameter $\mu_Y$, a gas-specific constant with viscosity dimensions [6]. The damping is given by

$$\gamma_{\text{YC}} = \frac{2\pi C S}{m(1+\omega^2\tau^2)^{3/4}}\left((1+\omega\tau)\cos\left(\frac{\tan^{-1}\omega\tau}{2}\right) - (1-\omega\tau)\sin\left(\frac{\tan^{-1}\omega\tau}{2}\right)\right)\sqrt{\frac{\omega\mu\rho_f}{2}}, \tag{2}$$

where $\mu$ is gas viscosity, $m$ is cantilever mass, $S$ is its top surface area, and $C$ is an overall scale factor of order unity, accounting phenomenologically for effective surface area and mass. Rescaling the measured damping $\gamma_m$ (after

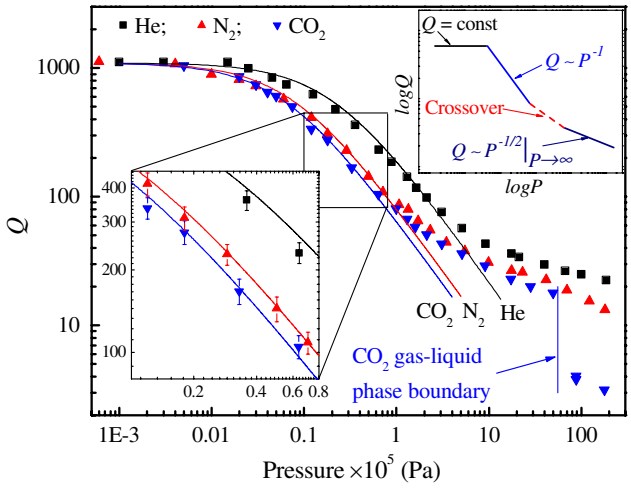


FIG. 2 (color online). $Q$ vs $P$ for cantilever 1 in three gases; solid lines show theoretical $Q$ in FMF assumption [Eq. (1)]. The right inset is a schematic of different damping regimes. The left inset is a magnified data fragment. The error is as shown, or less than the symbol size.

subtraction of the intrinsic dissipation) by $m/S\sqrt{\omega\mu\rho_f}$ allows us to plot simultaneously the results for all 19 devices, as a function of $\omega/P$ (Fig. 3). Squeeze film effects [10] are found to be appreciable only for the resonator number 19 (Table I) [18] and neglected in this plot. In this form, the normalized curve should be maximal when $\omega\tau \sim 1$. This allows a fit of the YCT to the data *en masse*, using two parameters, $\mu_Y$ (determining peak location) and $C$ (thick solid line in Fig. 3). For $N_2$ we find $\mu_Y^{N_2} \approx 0.6$ ms · Pa and $C^{N_2} \approx 2.7$ (the same $C$ value found in [13]). To illustrate the possible error in $\mu_Y^{N_2}$, Fig. 3 also shows fits using values of 0.25 ms · Pa (thin solid line), matching that suggested earlier [13] of 1850 ns · torr, and 1.0 ms · Pa (thin dotted line). Similarly, the values of $\mu_Y^{He} = 1.5$ ms · Pa with $C^{He} = 3.3 \pm 0.8$ and $\mu_Y^{CO_2} = 0.4$ ms · Pa with $C^{CO_2} = 2.2 \pm 0.5$ were found to be the best fits to the data in He and $CO_2$, respectively. In all cases, the model satisfactorily describes the low $P$ (high $\omega\tau$) FMF regime, and the crossover occurring at $\omega\tau \sim 1$, however, stops working at $\omega\tau \lesssim 0.1$, when the pressure becomes high and viscous added mass cannot be neglected (arrows in Fig. 3). An interesting trend is that the factor $C$ seems to become smaller as frequency is increased (the higher frequency devices tend to sit lower on the universal plot). Additionally, for shorter devices in He the YCT deviates from the data at somewhat higher values of $\omega\tau$ than for longer ones. These effects will be explored in future work.

Deconstructing in terms of $Q$ vs $P$, the $-1/2$ slope on the right-hand side of Fig. 3 corresponds to $Q \sim P^{-1}$ behavior as expected for FMF [19]. This can be confirmed on consideration of the $P$ dependence contained in the ordinate and abscissa ($P^{-1/2}$ and $P^{-1}$, respectively). The $Q \sim P^{-1/2}$ behavior at high $P$ would correspond to zero slope near the left-hand edge of the graph, except for that $\omega$ itself depends on $P$ at higher pressures. The added mass in a viscous boundary layer shifts $\omega$ to lower values at higher pressures, in our case, by as much as 30%. This has the effect of making the exponent of pressure dependence in the abscissa between $-1$ and $-1.5$ (depending on the amount of added mass compared to resonator mass) and $Q \sim P^{-1/2}$ dependence would manifest with some positive slope on the left edge of Fig. 3, which is observed in the data. This can explain why the YCT ceases to be valid as it underestimates the extra mass and its effect on $\omega$. It may be conceivable that the theory's validity could be extended into the viscous regime by accounting for the effects of added boundary layer mass.

We now turn to the meaning of $\mu_Y$. The inverse pressure dependence of $\tau$ is expected from proportionality to the molecular collision time in a gas $\tau_c$ [20]. $\mu_Y$ essentially "counts" gas molecular collisions until thermalization at a given pressure. Setting $\tau = \alpha\tau_c$ means

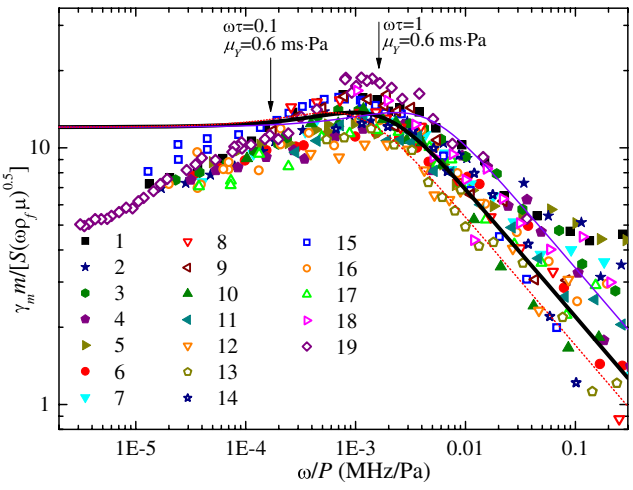


FIG. 3 (color online). Rescaled gas damping for all 19 samples in $N_2$ as a function of $\omega/P$. The thick solid line shows the best YCT fit [Eq. (2)] with $\mu_Y^{N_2} = 0.6$ ms · Pa. To demonstrate the spread in $\mu_Y$, the fit was repeated with $\mu_Y = 0.25$ ms · Pa (thin solid line); and with $\mu_Y = 1.0$ ms · Pa (thin dotted line).

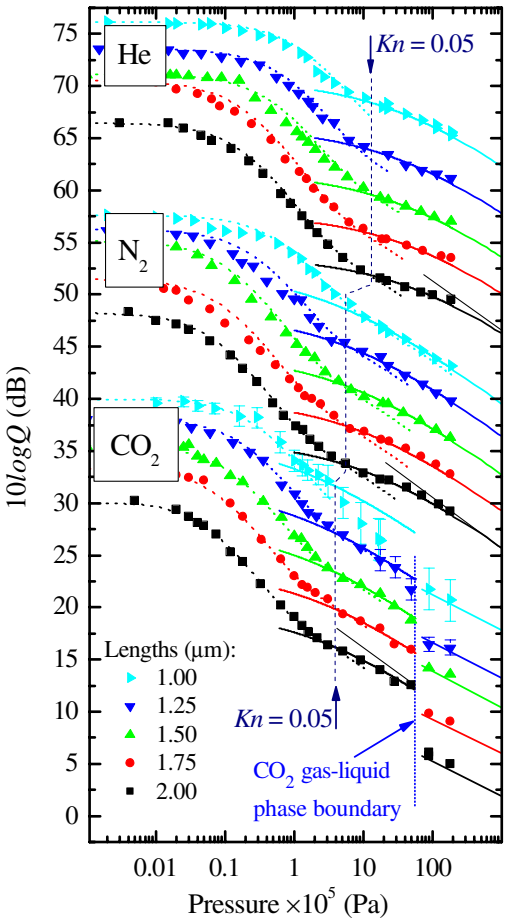


FIG. 4 (color online). Comparison of experiment with theoretical models for $Q$ vs $P$ of cantilevers 1–5 (symbols). Dotted lines show YCT fit [Eq. (2)], solid lines are MVS fits [Eq. (3)]. For clarity, the neighboring curves are offset by 3 dB; the offset between the different gases is 6 dB. The measurement errors are as marked or less than the size of the symbols. Straight solid lines at the high-$P$ end of the device 1 data in all gases are to show the $P^{-1/2}$ asymptote.

$\mu_Y = \alpha k_B \sqrt{TM}/(4D^2\sqrt{\pi R_g})$ where $M$ and $D$ are the mass and diameter of the gas molecule; $k_B$ and $R_g$ are the Boltzmann and universal gas constants. Working from the measured Yakhot parameters, this gives a characteristic collision number $\alpha$ for the 3 gases of 117, 42, and 33 for He, $N_2$, and $CO_2$, respectively. These numbers are surprisingly high; *a priori*, one might expect thermalization within the order of 10 collisions. Additionally, the reasons for gas dependency are not obvious. Without further data, we can only conjecture that a differing number of internal degrees of freedom might come into play.

Going back to $Q$ vs $P$ in all fluids, the listed above values for $\mu_Y$ and $C$ allowed us to fit $Q$ for all devices in the $P$ range from vacuum to the beginning of the viscous regime, where $\omega\tau \lesssim 0.1$ (dotted lines in Fig. 4).

To test the validity of Newtonian fluid models at the NEMS scale, we compare to a model known to be successful at larger sizes. Of the approaches that could be considered, the physical assumptions for MVS [9] are in the closest match to our case. According to MVS, a resonator can be substituted by a set of spheres whose radius $R$ is an adjustable parameter with value close to the device width. Then, the device $Q$ factor can be presented as

$$Q = \frac{m\omega}{6\pi\mu R + 1.5\pi R^2\sqrt{2\mu\rho_f\omega}}. \quad (3)$$

The solid lines in Fig. 4 show examples of fitting with MVS, using Eq. (3). It is remarkable that the viscous regime performance of all devices of the same width in all fluids was well approximated using the same value of parameter $R$: the widths 150, 250, and 1000 nm corresponded to $R$ of $137 \pm 8$, $179 \pm 10$, and $620 \pm 50$ nm, respectively. Amazingly, the same $R$ value remained valid in liquid $CO_2$ as well. Assuming linear relationship, one can phenomenologically write $R \approx 0.75(\pm 0.15)w$. Fitting both YCT and MVS on the same plot also allows direct observation of the validity regimes of each theory. Indeed as might be expected the transition to the viscous regime, and the theory validity changeover, appears to be at Kn $\sim$ 0.05 for most cases.

In summary, we investigated a number of NEMS resonators with varying linear dimensions in a widely varying pressurized fluid (He, $N_2$, $CO_2$) environment. The FMF regime extended to atmospheric pressure and above for these submicron devices. From vacuum to the start of the viscous regime (at pressures well above atmospheric), the YCT worked well for all cases; once in the viscous regime, the MVS Newtonian approach was most effective. The transition between the two was identified to occur at $\omega\tau \sim 0.1$ and Kn $\sim 0.05$.

This work was supported by NSERC, CIfAR, iCORE, CRC, and National Institute for Nanotechnology (NINT). Samples were fabricated at the Nanofab of University of Alberta, and SEM imaging was performed at NINT electron microscopy facility. N. L. was partially supported by the Avadh Bhatia Foundation.

*Present address: Micralyne Corp., Edmonton, Alberta, Canada.

[1] A. K. Naik, M. S. Hanay, W. K. Hiebert, X. L. Feng, and M. L. Roukes, Nature Nanotech. **4**, 445 (2009).
[2] T. P. Burg, M. Godin, S. M. Knudsen, W. Shen, G. Carlson, J. S. Foster, K. Babcock, and S. R. Manalis, Nature (London) **446**, 1066 (2007); J. Dorignac, A. Kalinowski, S. Erramilli, and P. Mohanty, Phys. Rev. Lett. **96**, 186105 (2006).
[3] Nanosensor networks are envisioned for down-well operation in the petroleum industry. See, for example, the Advanced Energy Consortium (www.beg.utexas.edu/aec/).
[4] W. E. Newell, Science **161**, 1320 (1968).
[5] R. B. Bhiladvala and Z. J. Wang, Phys. Rev. E **69**, 036307 (2004).
[6] V. Yakhot and C. Colosqui, J. Fluid Mech. **586**, 249 (2007).
[7] J. E. Sader, J. Appl. Phys. **84**, 64 (1998).
[8] C. Van Eysden and J. Sader, J. Appl. Phys. **101**, 044908 (2007).
[9] F. R. Blom, S. Bouwstra, M. Elwenspoek, and J. H. J. Fluitman, J. Vac. Sci. Technol. B **10**, 19 (1992); H. Hosaka, K. Itao, and S. Kuroda, Sens. Actuators A, Phys. **49**, 87 (1995); K. Kokubun, M. Hirata, H. Murakami, Y. Toda, and M. Ono, Vacuum **34**, 731 (1984).
[10] J. J. Blech, J. Lubr. Technol. **105**, 615 (1983); M. Andrews, I. Harris, and G. Turner, Sens. Actuators A, Phys. **36**, 79 (1993).
[11] M. Li, H. X. Tang, and M. L. Roukes, Nature Nanotech. **2**, 114 (2007).
[12] S. S. Verbridge, R. Ilic, H. G. Craighead, and J. M. Parpia, Appl. Phys. Lett. **93**, 013101 (2008).
[13] D. M. Karabacak, V. Yakhot, and K. L. Ekinci, Phys. Rev. Lett. **98**, 254505 (2007); K. L. Ekinci, D. M. Karabacak, and V. Yakhot, Phys. Rev. Lett. **101**, 264501 (2008).
[14] R. A. Bidkar, R. C. Tung, A. A. Alexeenko, H. Sumali, and A. Raman, Appl. Phys. Lett. **94**, 163117 (2009).
[15] N. Liu, F. Giesen, M. Belov, J. Losby, J. Moroz, A. E. Fraser, G. McKinnon, T. J. Clement, V. Sauer, W. K. Hiebert, and M. R. Freeman, Nature Nanotech. **3**, 715 (2008).
[16] O. Svitelskiy, N. Liu, V. Sauer, K.-M. Cheng, E. Finley, M. Belov, M. R. Freeman, and W. K. Hiebert, Rev. Sci. Instrum. **79**, 093701 (2008).
[17] A. N. Cleland, *Foundations of Nanomechanics* (Springer, Berlin, 2003).
[18] For this widest and longest device, the squeeze film effect should have added about 2 dB to the Yakhot theoretical curve around the maximum with smaller effect to the sides. This is slightly more than the experimental error. For other devices, the effect is within the device scatter.
[19] The increased scatter at the far right of the graph is influenced by increased sensitivity to the subtraction of $Q_{\text{intrinsic}}$ as $P$ shrinks.
[20] C. D. Stockbridge, in *Vacuum Microbalance Techniques* (Plenum, New York, 1966), Vol. 5, p. 147.